Nanoscale Advances

ROYAL SOCIETY OF CHEMISTRY

PAPER

View Article Online
View Journal | View Issue

Check for updates

Cite this: *Nanoscale Adv.*, 2025, **7**, 4183

Ultrasmall Bi/Bi_2O_3 nanoparticles as biocompatible and efficient CT imaging contrast agents†

Le T. T. Tam, [ab] Duong T. Ngoc,[c] Nguyen T. N. Linh,[d] Le T. Tam, [e] Nguyen V. Dong,[f] Nguyen T. Yen,[b] Nguyen T. Suong,[e] Ngo T. Dung *[b] and Le T. Lu [ab]

Computed tomography (CT) imaging is a widely used diagnostic tool, but conventional iodine-based contrast agents suffer from limitations such as short circulation time and potential nephrotoxicity. In this study, we present a simple one-pot thermal decomposition method for synthesizing ultrasmall Bi/Bi_2O_3 nanoparticles (NPs) using a commercial $Bi(NO_3)_3$ precursor and a surfactant mixture of oleic acid and oleylamine. Oleylamine acts as a reducing agent, facilitating the conversion of Bi^{3+} to metallic Bi, while the Bi_2O_3 oxide layer is controlled by adjusting the oleic acid-to-oleylamine ratio. To enhance biocompatibility and aqueous dispersibility, the NPs are further modified with polyacrylic acid (PAA), resulting in Bi/Bi_2O_3@PAA NPs with an ultra-small size, high Bi content, and stability. X-ray attenuation measurements reveal that Bi/Bi_2O_3@PAA NPs exhibit superior contrast enhancement compared to the traditional iodine-based contrast agents, with increasing efficacy at higher tube voltages. Given their facile synthesis, excellent biocompatibility, and outstanding imaging performance, Bi/Bi_2O_3@PAA NPs hold significant promise as next-generation CT contrast agents for clinical applications.

Received 22nd April 2025
Accepted 27th May 2025

DOI: 10.1039/d5na00389j

rsc.li/nanoscale-advances

Open Access Article. Published on 28 May 2025. Downloaded on 2/18/2026 10:23:10 AM.
This article is licensed under a Creative Commons Attribution-NonCommercial 3.0 Unported Licence.

Introduction

Computed tomography (CT) imaging is an indispensable tool in modern diagnostic medicine, providing high spatial resolution and detailed visualization of internal structures.[1,2] However, the inherent low contrast of soft tissues in CT scans necessitates the use of contrast agents to create distinct images of tissues with similar contrast. Currently, iodinated compounds such as iohexol, ioversol or iopamidol are the most commonly used contrast agents due to their strong X-ray attenuation and water solubility.[3,4] Despite their effectiveness, these agents have significant limitations, including short circulation times, nonspecific distribution, the necessity of high doses, hypersensitivity reactions, and potential nephrotoxicity, especially in patients with pre-existing kidney conditions.[5–8] These challenges drive the ongoing search for safer and more effective alternatives to traditional iodine-based agents.

Recent advancements in nanotechnology have enabled the development of CT contrast agents based on metal NPs such as gold (Au), bismuth (Bi), and gadolinium (Gd), offering an alternative to traditional iodine-based agents.[4,8–12] These NPs exhibit superior X-ray absorption due to their high atomic numbers.[2] Among them, bismuth (Bi), the heaviest non-radioactive metal, has emerged as a particularly promising candidate due to its excellent X-ray attenuation ($Z = 83$) and ability to provide higher contrast than iodine and other high-Z materials in CT imaging. This is attributed to its high K-edge value (90.5 keV) and large X-ray attenuation coefficient (5.74 $cm^2\ g^{-1}$ at 100 keV).[13] Additionally, bismuth is the most cost-effective among heavy metal and is widely recognized for its biosafety.[14–16] A series of bismuth-containing medications have been extensively used for treating gastrointestinal disorders, hypertension, infections, cancers, and inflammation, further supporting its potential as a high-performance CT contrast agents (CAs).

Various Bi-based nanomaterials have been explored as next-generation CT CAs, including small-molecule chelates such as Bi-DTPA,[17–19] Bi-DOTA[20] as well as NPs like metallic Bi,[2,21] bismuth oxide (Bi_2O_3),[22] and bismuth sulfide (Bi_2S_3).[23–26] Among these, metallic Bi NPs are particularly attractive as CT contrast agents due to their high bismuth atom density, which enables strong X-ray attenuation within a relatively small volume. For example, Li *et al.* developed PEGylated metallic Bi nanocrystals (Bi-PEG NCs) using a chemical reduction method.[11] These Bi-PEG NCs exhibited excellent CT contrast enhancement, good

[a]*Graduate University of Science and Technology, Vietnam Academy of Science and Technology, 18 Hoang Quoc Viet, Hanoi, Vietnam*
[b]*Institute of Materials Science, Vietnam Academy of Science and Technology, 18 Hoang Quoc Viet, Hanoi, Vietnam. E-mail: ngodunght@gmail.com*
[c]*Hanoi National University of Education, 136 Xuan Thuy, Cau Giay, Hanoi, Vietnam*
[d]*Thai Nguyen University of Sciences, Tan Thinh Ward, Thai Nguyen City 25000, Thai Nguyen, Vietnam*
[e]*Vinh University, 182 Le Duan, Vinh City, Vietnam*
[f]*Hoan My Vinh Hospital, 99 Pham Đinh Toai, Vinh City, Vietnam*

† Electronic supplementary information (ESI) available. See DOI: https://doi.org/10.1039/d5na00389j

© 2025 The Author(s). Published by the Royal Society of Chemistry

Open Access Article. Published on 28 May 2025. Downloaded on 2/18/2026 10:23:10 AM. This article is licensed under a Creative Commons Attribution-NonCommercial 3.0 Unported Licence.

biocompatibility and safety. Similarly, Yang *et al.* synthesised Bi NPs using Bi(III) acetate as a precursor in a mixed solution of oleic acid and 1-dodecanethiol.[27] The resulting Bi NPs were coated with 1,2-dilauroyl-*sn-glycero*-3-phosphocholine (Bi@DLPC NPs) through ultrasonic treatment, achieving a uniform size of 47 ± 3 nm. The CT imaging properties of Bi@DLPC NPs were concentration-dependent, with signal intensity and HU values significantly increasing as the concentration rose from 0.313 to 5 mg mL^{-1}. Tarighatnia *et al.* synthesized Bi NPs *via* thermal decomposition and subsequently functionalized them with targeting biomolecules such as MUC16, leading to enhanced X-ray attenuation through specific targeting effects.[28,29] Compared to gold NPs (Au NPs), which share similar synthesis versatility and tunability in size and morphology, Bi NPs offer a more cost-effective alternative, being approximately 2000 times less expensive.[30,31]

Despite these advantages, Bi NPs face several challenges, including poor stability, large particle sizes, labor-intensive postsynthetic surface modifications, and limited targeting properties.[11,27] For instance, bare Bi NPs tend to undergo rapid oxidation and aggregation in biological environments, limiting their practical application.[11] Meanwhile, Bi_2O_3 and Bi_2S_3 NPs have gained increasing attention due to their high stability, adjustable cytotoxicity, and cost-effective synthesis, making them promising candidates for CT diagnostic applications.[32] However, a key limitation of these compounds is their lower bismuth atom concentration per particle due to the presence of oxygen or sulfur. Furthermore, Bi_2S_3 suffers from instability in aqueous media, where hydrolysis can lead to the release of toxic hydrogen sulfide gas, posing safety concerns.

In this study, we propose a simple and effective synthesis method for ultrasmall Bi/Bi_2O_3 NPs *via* a one-pot thermal decomposition of a commercial $Bi(NO_3)_3$ precursor in the presence of a surfactant mixture containing oleic acid and oleylamine. In this process, oleylamine acts as a reducing agent to efficiently convert Bi^{3+} to metallic Bi, while the formation of the Bi_2O_3 oxide layer is controlled by adjusting the oleic acid-to-oleylamine ratio. Further surface modification of $Bi@Bi_2O_3$ NPs can be easily achieved with polyacrylic acid (PAA) to make the sample hydrophilic and biocompatible. The obtained Bi/Bi_2O_3@PAA NPs exhibited an ultra-small size (3 nm), outstanding water solubility, high Bi content and biocompatibility. The X-ray attenuation ability of Bi/Bi_2O_3@PAA NPs is more than 2-fold higher than that of some iodine-based clinical contrast agents, and the superiority becomes increasingly pronounced with increasing tube voltage.

Compared to previously reported methods, the proposed strategy offers several distinct advantages for the large-scale production of high-performance CT contrast agents: (i) a simple and cost-effective synthesis utilizing commercially available reagents, eliminating the need of the specially designed precursors or multi-step procedures; (ii) the synthesis of ultrasmall, monodisperse NPs with tunable structure and composition by adjusting OA/OLA ratio; and (iii) straightforward surface modification with ligands such as PAA, resulting in enhanced aqueous stability and biocompatibility. These advantages underscore the high potential of Bi/Bi_2O_3@PAA NPs as promising next-generation CT contrast agents.

Experimental

Chemicals

All used chemicals are at least analytical grade without further purification. Bismuth nitrate pentahydrate (99.99%), dibenzyl ether (90%), 1-octadecene (90%), oleic acid (OA) (99%), oleylamine (OLA) (70%), *N*,*N*-dimethylformamide (DMF), nitrosonium tetrafluoroborate ($NOBF_4$, 95%), polyacrylic acid (PAA, M_w = 1800), ethanol (≥96%), *n*-hexane (99%) and chloroform (≥99%) were purchased from Sigma-Aldrich.

Synthesis of Bi/Bi_2O_3 NPs

Ultrasmall Bi/Bi_2O_3 NPs were synthesized *via* a thermal decomposition method. Initially, 10 mmol of $Bi(NO_3)_3 \cdot 5H_2O$ was dissolved in a 100 mL three-neck round-bottom flask containing a surfactant mixture of OA and OLA in a 2 : 1 molar ratio. 40 mL solvent mixture of octadecene and dibenzyl ether in a 1 : 1 volume ratio was then added to the flask. The reaction mixture was stirred at 600 rpm and heated to 100 °C for 30 minutes under a nitrogen atmosphere to remove air and prevent subsequent oxidation of the NPs. The temperature was subsequently increased to 200 °C and maintained for 1 hour. Following this step, the mixture was further heated to 300 °C and held for an additional hour. After the reaction, the solution was allowed to cool naturally to room temperature. The synthesised NPs were collected, washed 2–3 times with a mixture of *n*-hexane/ethanol (1 : 1), precipitated by centrifugation, and then dispersed in *n*-hexane.

Surface modification of Bi/Bi_2O_3 NPs with PAA

Bi/Bi_2O_3 NPs were surface modified with PAA through ligand exchange according to the following procedure: firstly, 10 mL of a Bi/Bi_2O_3 NPs solution was sonicated for 3–5 minutes to ensure uniform dispersion. Subsequently, 10 mL of a chloroform/DMF solution containing 0.01 M $NOBF_4$ was added to the NP solution at room temperature. The mixture was sonicated until a precipitate formed, typically within 5 minutes. The NPs were purified by washing multiple times with a toluene/hexane mixture (1 : 1 volume ratio) followed by centrifugation at 12 000 rpm for 8–10 minutes.

The purified NPs were then redispersed in 10 mL of an aqueous solution containing PAA. This mixture was continuously stirred at room temperature for 8 hours to facilitate surface modification. After the reaction, the product was washed thoroughly with distilled water until the solution reached a neutral pH (pH = 7). The resulting Bi/Bi_2O_3@PAA NPs are good dispersible in water, making them suitable for further applications.

Characterisation

Morphology of Bi/Bi_2O_3 NPs was studied by transmission electron microscopy (TEM, JEM1010-JEOL). The phase structure and composition of the NPs were determined by X-ray

© 2025 The Author(s). Published by the Royal Society of Chemistry

Open Access Article. Published on 28 May 2025. Downloaded on 2/18/2026 10:23:10 AM.
This article is licensed under a Creative Commons Attribution-NonCommercial 3.0 Unported Licence.

diffraction analysis. UV-vis (Jasco V-670) spectrometer was employed to record absorption spectra of the samples. The distribution of the elements within the Bi/Bi_2O_3 samples were determined by the Energy Dispersive X-ray spectroscopy (EDX) analysis on the Hitachi S-4800 FESEM equipped. X-ray photoelectron spectroscopy measurements (XPS, Thermo Fisher) were carried out using monochromatic Al Kα radiation ($h\nu$ = 1486.6 eV). FT-IR spectroscopy (Nicolet 6700) and TGA (Nezsch, Germany) analyses were used to characterise the surface structure of Bi/Bi_2O_3 NPs. Dynamic light scattering (DLS) and zeta potential measurements were used to investigate the distribution and stability of Bi/Bi_2O_3 NPs in aqueous medium. ICP-MS was obtained on an Agilent Technologies, Japan.

Cell viability measurement

The cytotoxicity of Bi/Bi_2O_3 NPs was evaluated using the methyl thiazolyl tetrazolium (MTT) assay with Vero cells (kidney cells from the African green monkey) as a model. First, Vero cells (1.5×10^5) were seeded in a 96-well plate and incubated at 37 °C with 5% CO_2 for 24 hours in Dulbecco's Modified Eagle's Medium (DMEM) supplemented with 10% fetal bovine serum (FBS) and 1% penicillin/streptomycin. The medium was then replaced with fresh medium containing Bi/Bi_2O_3 NPs at concentrations of 12.5, 25, 50, 100, and 200 μg mL^{-1}, followed by incubation for 72 hours. Cell viability was assessed by adding 20 μL of MTT solution to each well and incubating for 4 hours at 37 °C. The resulting formazan crystals were dissolved in dimethyl sulfoxide (DMSO, Sigma-Aldrich), and optical density was measured at 540 nm using a Tecan Spark microplate reader (Männedorf, Switzerland).

CT phantom image measurements

The CT imaging was performed using 128-Somatom perspective CT scanner (Siemens, Germany) with the following imaging parameters: source voltage 80–130 kV, 80 mAs, slice thickness 0.75 mm, field of view DFOV x–y 290×320 mm^2, matrix size 532×532. Samples, dispersed in water with different metal concentrations (agarose 2%, 2, 4, 6, 9 and 12 mM), were placed in 2 mL wells and positioned in a custom-made scanning support. X-ray attenuation intensity was assessed by loading digital CT images into a standard display program. For each sample, a uniform circular region of interest (ROI) with an area of approximately 0.3 cm^2 was consistently selected at the center of the well to minimize variability from edge effects or positioning differences. Contrast enhancement was quantified in Hounsfield units (HU) for each sample at different metal concentrations. The measurements (ROIs in cm^2) were obtained using eFilm workstations (Merge Healthcare, Chicago, IL, USA) and used for image reconstruction. Prior to scanning, quality control procedures were performed on the CT system to ensure accurate and reproducible measurements.

Results and discussion

In this study, we developed a straightforward strategy to synthesise ultra-small Bi/Bi_2O_3 NPs through the thermal decomposition of the commercial precursor $Bi(NO_3)_3$ in the presence of oleic acid (OA) and oleylamine (OLA) as surfactants. Notably, OLA also served as a reducing agent, efficiently converting Bi^{3+} to metallic Bi. Meanwhile, the surface oxidation level of Bi NPs was controlled by adjusting the OA/OLA ratio during the synthesis process. The surface of the Bi/Bi_2O_3 NPs was subsequently modified with the polyacrylic acid (PAA) using a ligand exchange method. The synthesis and surface modification process of Bi/Bi_2O_3 NPs are illustrated in Scheme 1. This scheme also includes photographs of the NP solutions before and after ligand exchange, visually indicating their distinct physicochemical properties. The dark brown solution in the upper non-polar phase (*n*-hexane) represents the as-synthesized hydrophobic Bi/Bi_2O_3 NPs, stabilized by OA/OLA ligands. In contrast, the milky white solution in the lower aqueous phase corresponds to the PAA-coated NPs, suggesting successful ligand exchange and enhanced colloidal stability in water. This clear visual distinction provides qualitative evidence of successful surface modification and indicates the effectiveness of the strategy in improving NP dispersibility and chemical compatibility for potential biomedical applications.

Fig. 1a and b display TEM image and size distribution of as-synthesised Bi/Bi_2O_3 NPs. The TEM image revealed that the synthesised Bi/Bi_2O_3 NPs are monodisperse and spherical with a small size of ~3 nm. Additionally, a high-resolution TEM image and a fast Fourier transform (FFT) analysis of a single nanoparticle (Fig. 1c) confirm the presence of a distinct lattice fringe measured at 2.25 Å, corresponding to the (110) diffraction planes of the rhombohedral structure of bismuth.

To further evaluate the phase composition and crystallinity of the Bi/Bi_2O_3 NPs, X-ray diffraction (XRD) analysis was performed (Fig. 1d). The diffraction peaks align well with standard patterns for rhombohedral metallic bismuth (PDF 01-085-1329) and tetragonal β-Bi_2O_3 (PDF 01-074-1374), confirming the formation of a Bi/Bi_2O_3 hybrid structure. The presence of Bi_2O_3 suggests partial surface oxidation of bismuth during synthesis, while the absence of impurity peaks indicating the high purity of the synthesised NPs. The sharp and well-defined diffraction peaks further demonstrate the crystalline nature of the sample, which is consistent with previously reported XRD data for ultra-small Bi NPs.[21,33]

The extent of oxidation of Bi NPs was found to be significantly influenced by the OA/OLA ratio, as evidenced by the XRD and TEM analyses (Fig. S1 and S2†). In OA-rich condition (OA/OLA = 3/1), the elevated concentration of OA promoted significant oxidation of bismuth, leading to the predominant formation of Bi_2O_3 NPs with an average size of 3.3 ± 0.5 nm. In contrast, in OLA-rich liquids (OA/OLA = 1/3), OLA served as the dominant reducing agent, effectively suppressing oxidation and promoting the formation of metallic Bi NPs with the size of 2.9 ± 0.4 nm. At an intermediate OA/OLA ratio of 2/1, a controlled oxidation process was achieved, leading to the formation of Bi/Bi_2O_3 hybrid NPs while maintaining a small and uniform particle size (3.0 ± 0.4 nm). These findings demonstrate the pivotal role of the OA/OLA ratio in tuning the oxidation state of the synthesised NPs.

Open Access Article. Published on 28 May 2025. Downloaded on 2/18/2026 10:23:10 AM.
This article is licensed under a Creative Commons Attribution-NonCommercial 3.0 Unported Licence.

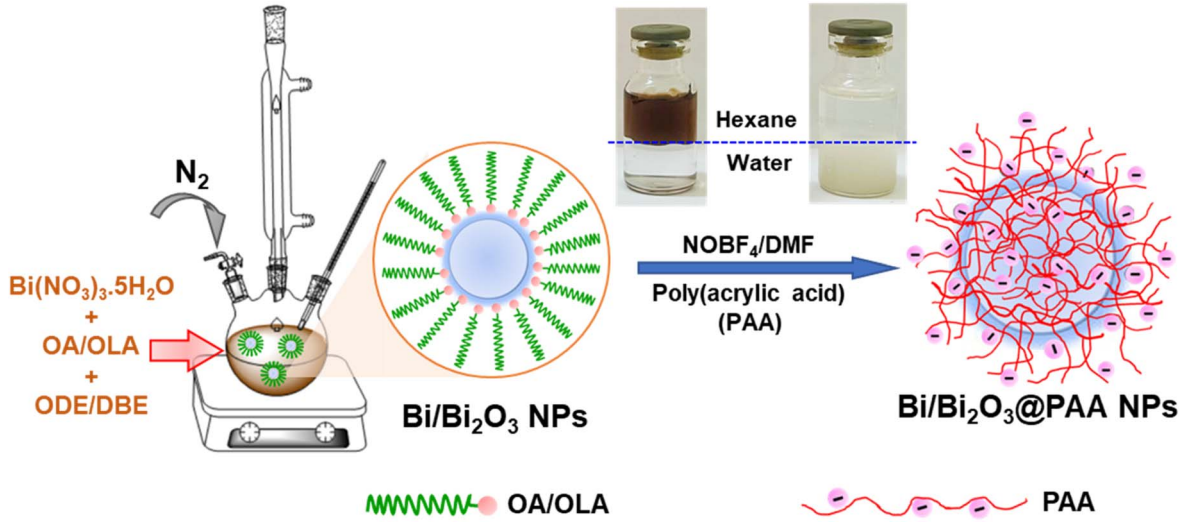

Scheme 1 Schematic illustration of one-pot synthesis of Bi/Bi_2O_3 NPs as a high-performance CT contrast agent.

To quantitatively determine the phase composition, Rietveld refinement was performed using the FullProf software (pseudo-Voigt function). The analysis revealed that the sample prepared at OA/OLA ratio of 2 : 1 consists of 75.1% metallic Bi and 24.9% Bi_2O_3, indicating that this ratio achieves a well-balanced composition between Bi and Bi_2O_3. This precise control over the oxidation state is essential for tuning the physicochemical properties of the NPs, thereby enhancing their potential in biomedical applications such as CT imaging.

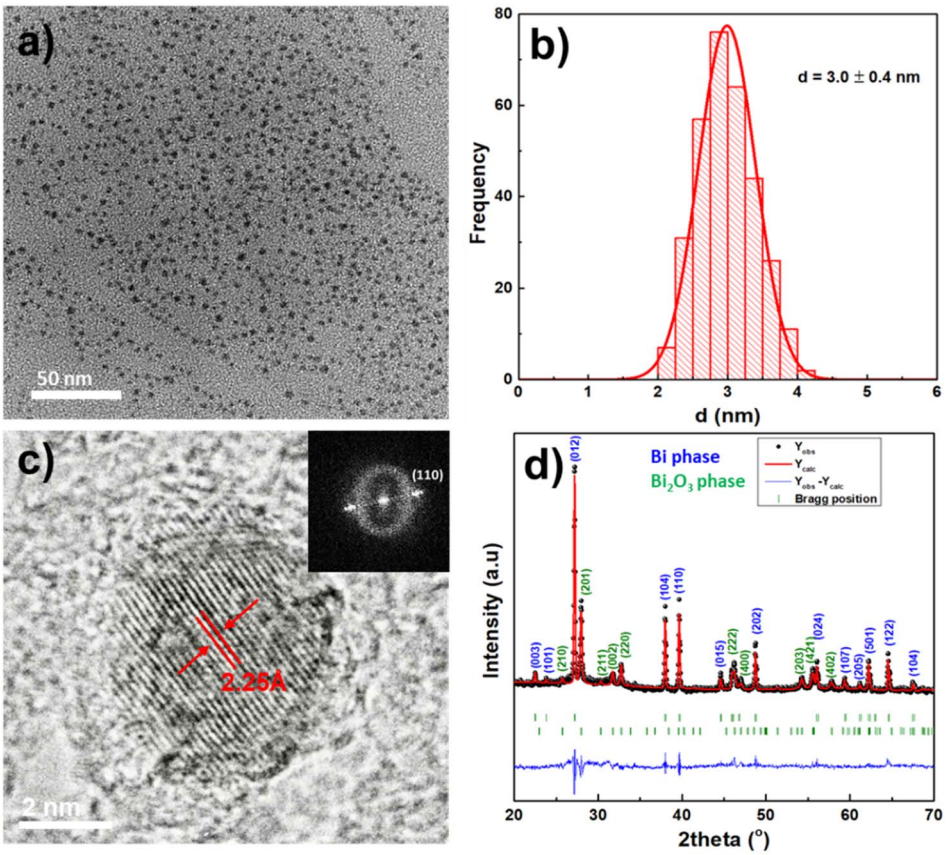

Fig. 1 (a) TEM image, (b) size distribution of Bi/Bi_2O_3 NPs, (c) HRTEM image of Bi/Bi_2O_3 NPs with an inset FFT image and (d) Rietveld refinement profile of XRD data of as prepared Bi/Bi_2O_3 NPs. The black line correspond to the experimental data and the red line is for the Rietveld refinement fit. The lower curve is the difference between the observed and calculated at each step.

© 2025 The Author(s). Published by the Royal Society of Chemistry

Open Access Article. Published on 28 May 2025. Downloaded on 2/18/2026 10:23:10 AM.
This article is licensed under a Creative Commons Attribution-NonCommercial 3.0 Unported Licence.

To further characterise the synthesised Bi/Bi_2O_3 NPs, UV-vis spectroscopy was also conducted. The optical transmission spectra of the Bi/Bi_2O_3 NPs solution, recorded in wavelength range of 200 and 800 nm, exhibited a distinct absorbance peak at 273 nm, as shown in Fig. 2a. This peak is characteristic of Bi_2O_3 NPs and is consistent with previous reports,[34] thereby confirming the presence of the Bi_2O_3 phase within the hybrid structure.

The optical band gap energy (E_g) of Bi/Bi_2O_3 NPs is calculated using the Tauc equation:[35,36]

$$(\alpha h\nu) = A(h\nu - E_g)^n$$

where α, h, ν, E_g and A are absorption coefficient, Planck's constant, light frequency, band gap energy, and a constant, respectively.

For Bi/Bi_2O_3 NPs, a value of $n = 2$ was used in the Tauc equation, indicating a direct allowed transition. By extrapolating the linear portion of the Tauc plot to the x-axis, the optical band gap energy was determined to be 3.88 eV (Fig. 2b). This value is good agreement with previously reported values for Bi_2O_3, which range from 2 to 3.96 eV.[35–38] The observed increase in band gap energy compared to bulk material is likely due to the quantum confinement effect, which becomes significant as the particle size decreases to the nanoscale.[35]

EDX analysis (Fig. 3) confirms the presence of Bi, O, and C elements, where C originating from surfactant molecules on the NPs surface. EDX elemental mapping (Fig. 2c and d) shows a dominant Bi signal alongside a relatively weak O signal, supporting the formation of the Bi/Bi_2O_3 structure, consistent with the XRD results. Furthermore, the elemental mapping demonstrates the homogeneous distribution of Bi and O throughout the sample.

Further insights into the surface chemical composition of the Bi/Bi_2O_3 NPs were obtained *via* XPS analysis, as shown in Fig. 4. The wide-scan XPS survey spectrum (Fig. 4a) confirmed the presence of Bi, O and C elements on the NPs surface. The high resolution C 1s spectrum (Fig. 4b) was deconvoluted into three peaks at binding energies of 284.7 eV, 285.1 eV and 288 eV, corresponding to C–C/C=C, C–O and O–C=O bonds, respectively.

The Bi 4f spectrum (Fig. 4c) exhibits two distinct doublets. The peak at 158.6 eV and 163.9 eV are assigned to metallic Bi (Bi^0), while the peaks at 159.1 eV and 164.4 eV are associated with Bi^{3+} species, originating from Bi_2O_3 phase. The coexistence of Bi^0 and Bi^{3+} signals provide evidence of partial surface oxidation, consistent with previous reports.[29,39,40] These results further suggest that Bi_2O_3 is effectively anchored to the surface shell of the Bi NPs, forming a core–shell Bi/Bi_2O_3 hybrid nanostructure.

In Fig. 4d, the high resolution O 1s spectrum was deconvoluted into two peaks located at 530.7 eV and 531.8 eV. These binding energies are attributed to the lattice oxygen in bismuth oxide and the surface-adsorbed oxygen species, respectively.[41]

The as-synthesised Bi/Bi_2O_3 NPs exhibited hydrophobicity due to the presence of OA and OLA on their surface. To enable biomedical application, a surface modification *via* ligand exchange was performed to render the NPs hydrophilic. The surface modification process was monitored using FT-IR spectroscopy, as shown in Fig. 5a. The FTIR spectrum of OA/OLA-coated Bi/Bi_2O_3 NPs displayed strong symmetric and asymmetric C–H stretching vibrations at 2850 cm^{-1} and 2920 cm^{-1}, respectively, characteristic of the alkyl chain of OA and OLA. A broad absorption band at 3435 cm^{-1} corresponds to the vibration of O–H. Additional peaks observed at 1463 cm^{-1}, 1542 cm^{-1} and 1635 cm^{-1}, are attributed to the $-CH_2-$ bending, and the symmetric and asymmetric stretching vibration of the carboxylate (COO^-) group, respectively, indicating the coordination of OA and OM molecules to the NPs surface, possibly as OA/OLA complexes.[42–44]

Upon treatment with $NOBF_4$, the FTIR spectrum of BF_4^--coated Bi/Bi_2O_3 NPs, reveals the disappearance of these characteristic bands, alongside the appearance of new peaks at 1084 cm^{-1} and 1643 cm^{-1}, which are assigned to $BF4^-$ anions and C=O stretching vibrations from DMF solvent molecules, respectively. These spectral changes confirm the successful removal of OA/OLA ligands and their replacement with $BF4^-$ anions.

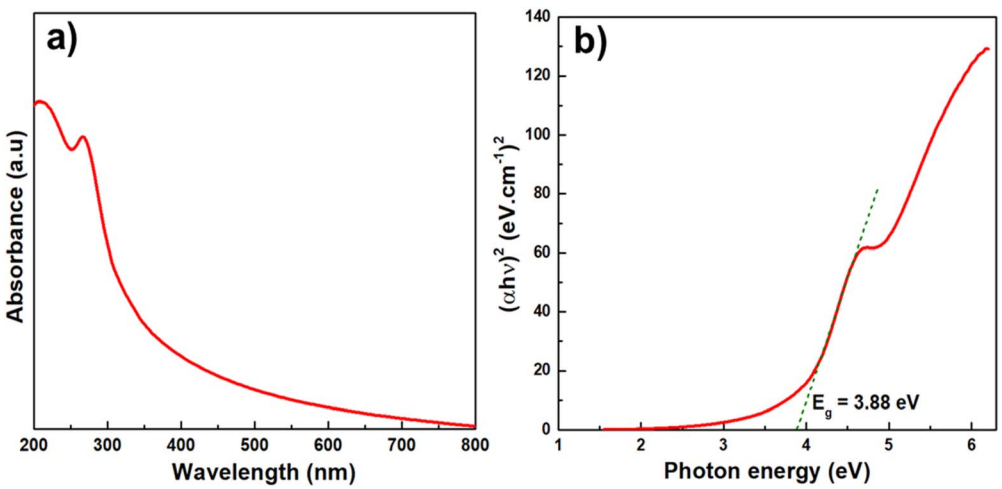

Fig. 2 (a) UV-vis absorption spectrum and (b) the optical band gap energy (E_g) of the Bi/Bi_2O_3 NPs.

Open Access Article. Published on 28 May 2025. Downloaded on 2/18/2026 10:23:10 AM.
This article is licensed under a Creative Commons Attribution-NonCommercial 3.0 Unported Licence.

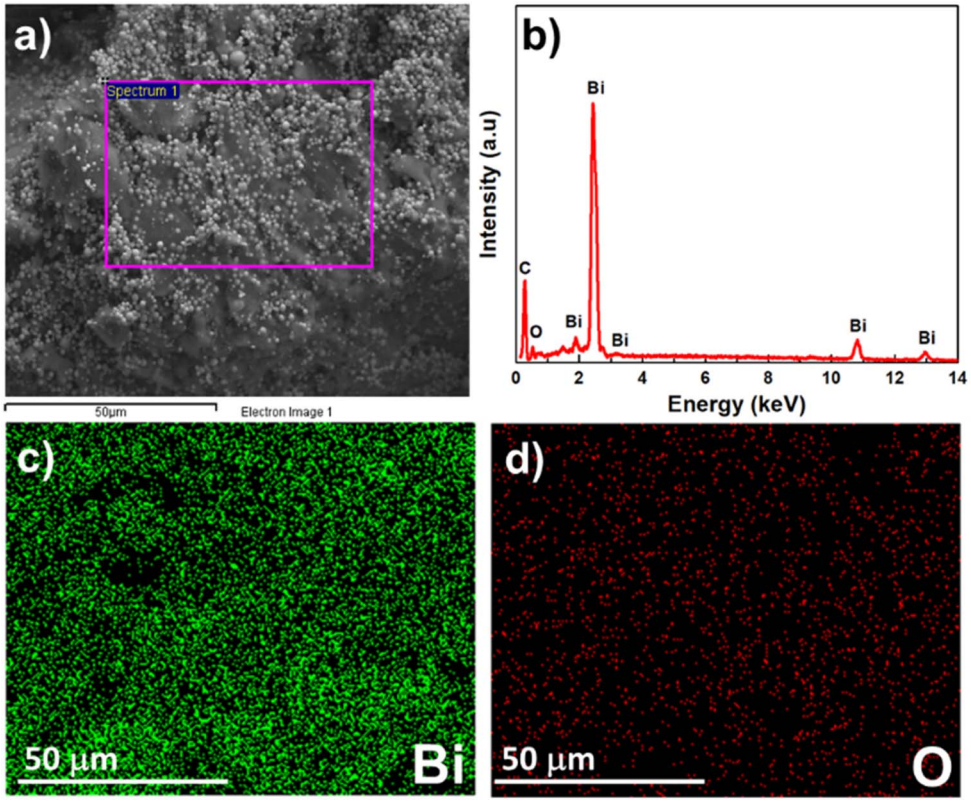

Fig. 3 (a) SEM image, (b) EDX spectrum and (c and d) elemental mapping of the Bi/Bi_2O_3 NPs.

Following PAA modification, the FTIR spectrum of PAA-coated Bi/Bi_2O_3 NPs exhibited a peak at 1712 cm^{-1}, corresponding to the C═O stretching vibration of free carboxylic acid groups (COOH). A strong band at 1553 cm^{-1} is attributed to the C–O stretching of carboxylate ions, indicating partial deprotonation of the PAA at neutral pH, where both protonated and deprotonated carboxyl groups coexist.[45] Additionally, weak peaks observed at 550 cm^{-1} and 462 cm^{-1} correspond to Bi–O stretching vibrations, further confirming the presence of Bi_2O_3 in the NP structure.[46,47]

To further confirm the successful coating of PAA onto Bi/Bi_2O_3 NPs, thermogravimetric analysis (TGA) was performed. The TGA curves of the NPs before and after PAA modification are presented in Fig. 5b. For OA/OM-coated Bi/Bi_2O_3 NPs, a substantial weight loss is observed between 200 and 550 °C, which is attributed to the decomposition of OA and OM molecules. After PAA modification, the onset of decomposition shifts to a higher temperature (260 °C), suggesting stronger binding interactions of PAA molecules to the particle surface, consistent with the FTIR results.

The colloidal stability of Bi/Bi_2O_3@PAA NPs was evaluated using DLS analysis, and the results are presented in Fig. 6. As shown in Fig. 6a, the NPs exhibit a narrow hydrodynamic size distribution with an average hydrodynamic diameter of 36.8 nm, indicating uniform dispersion of Bi/Bi_2O_3@PAA NPs. The zeta potential measurement (Fig. 6b) reveals a surface charge of −38.8 mV, which is attributed to the presence of negative charged carboxyl groups from PAA coating. This strong electrostatic repulsion contributes to enhanced colloidal stability by effectively preventing NP aggregation.

Further investigation of size distribution under varying pH conditions reveals that the NPs remain stable across a wide pH range (2 to 12), while a highly acidic environment (pH = 1) induces a significant change in particle size, suggesting pH-dependent surface interactions (Fig. 6c). After two months of storage, both the hydrodynamic size and zeta potential remain nearly unchanged, confirming the long-term colloidal stability of the NPs (Fig. 6d).

The colloidal stability of the Bi/Bi_2O_3@PAA NPs is further supported by the visual appearance of their dispersions at different concentrations. At high concentration, the solution exhibits a milky white appearance. Notably, no visible aggregation or sedimentation was observed after two months of storage, indicating excellent long-term colloidal stability under ambient conditions. Upon dilution to a concentration of 5 mM, the solution becomes optically transparent, consistent with the expected behavior of ultrasmall NPs, as reported in the literature. These findings suggest the effectiveness of PAA surface modification in enhancing the colloidal stability of Bi/Bi_2O_3 NPs, supporting their potential for imaging diagnostic applications.

In vitro toxicity assessment

The biocompatibility of Bi/Bi_2O_3@PAA NPs was evaluated through MTT assay, measuring the viability of Vero cells after 72

© 2025 The Author(s). Published by the Royal Society of Chemistry

Open Access Article. Published on 28 May 2025. Downloaded on 2/18/2026 10:23:10 AM.
This article is licensed under a Creative Commons Attribution-NonCommercial 3.0 Unported Licence.

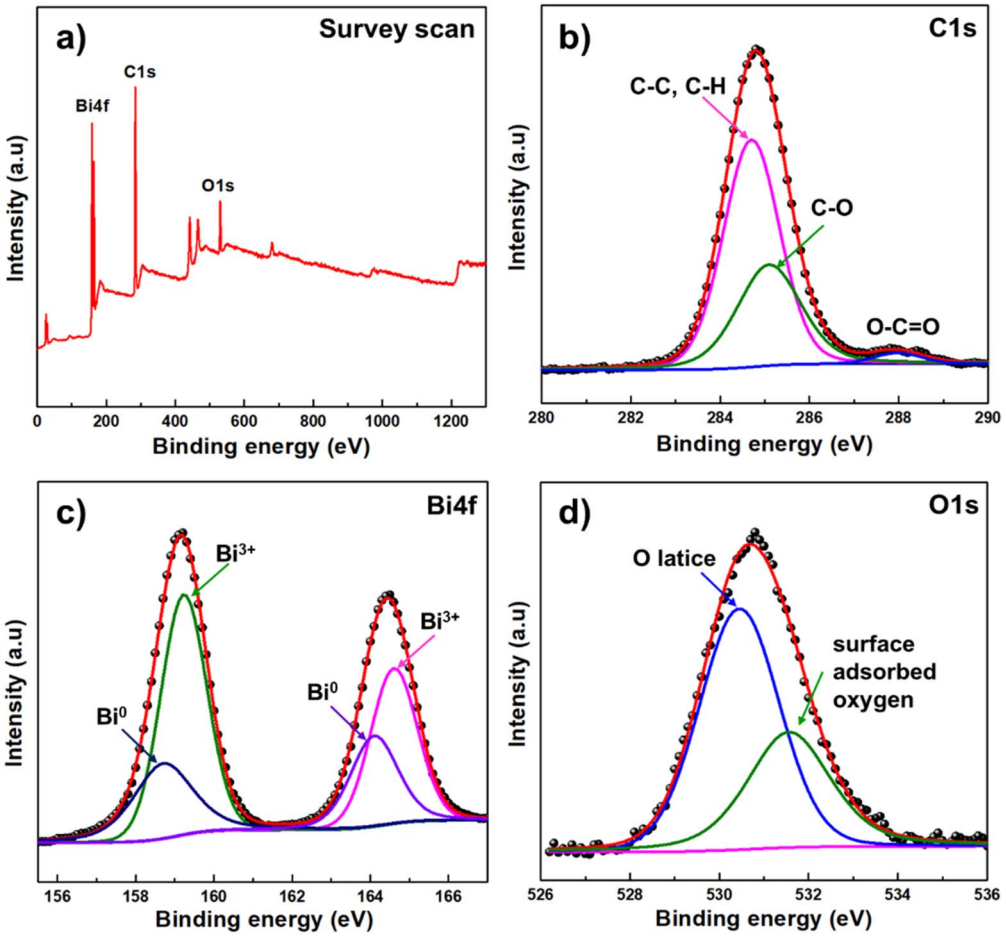

Fig. 4 XPS spectra of Bi/Bi_2O_3 NPs: (a) scan survey; high-resolution XPS spectra of (b) C 1s, (c) Bi 4f and (d) O 1s.

hours of incubation with varying NP concentrations (Fig. 7). The results demonstrated that cell viability remained above 72% even at concentrations as high as 200 μg mL^{-1}, indicating low cytotoxicity and suitable biocompatibility of the NPs for potential *in vivo* CT applications.

Performance on CT imaging *in vitro*

The CT imaging capability of Bi/Bi_2O_3@PAA NPs was evaluated *in vitro* using CT phantom imaging. Solutions with varying Bi concentrations (2, 4, 6, 9 and 12 mM) were imaged under tube voltages ranging from 80 to 130 kV. As shown in Fig. 8, Bi/Bi_2O_3@PAA NPs exhibited progressively enhanced brightness with

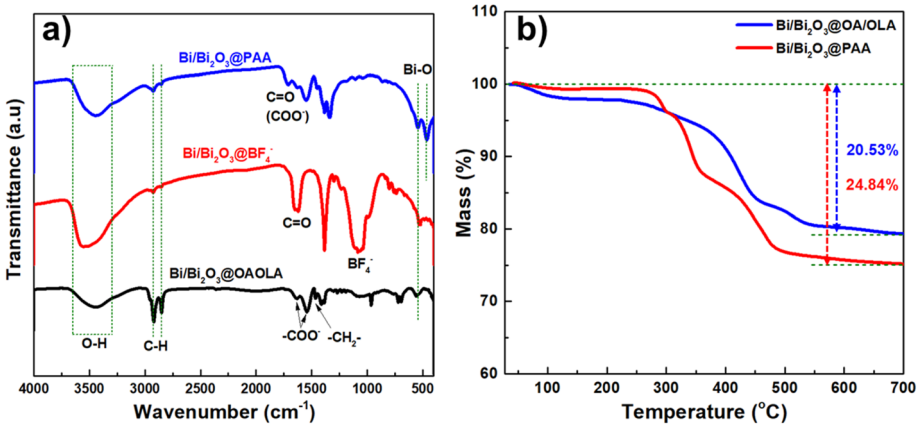

Fig. 5 (a) FTIR spectra and (b) thermogravimetric analysis (TGA) plots of Bi/Bi_2O_3 NPs before surface modification (Bi/Bi_2O_3@OA/OLA) and after modification with PAA.

Open Access Article. Published on 28 May 2025. Downloaded on 2/18/2026 10:23:10 AM.
This article is licensed under a Creative Commons Attribution-NonCommercial 3.0 Unported Licence.

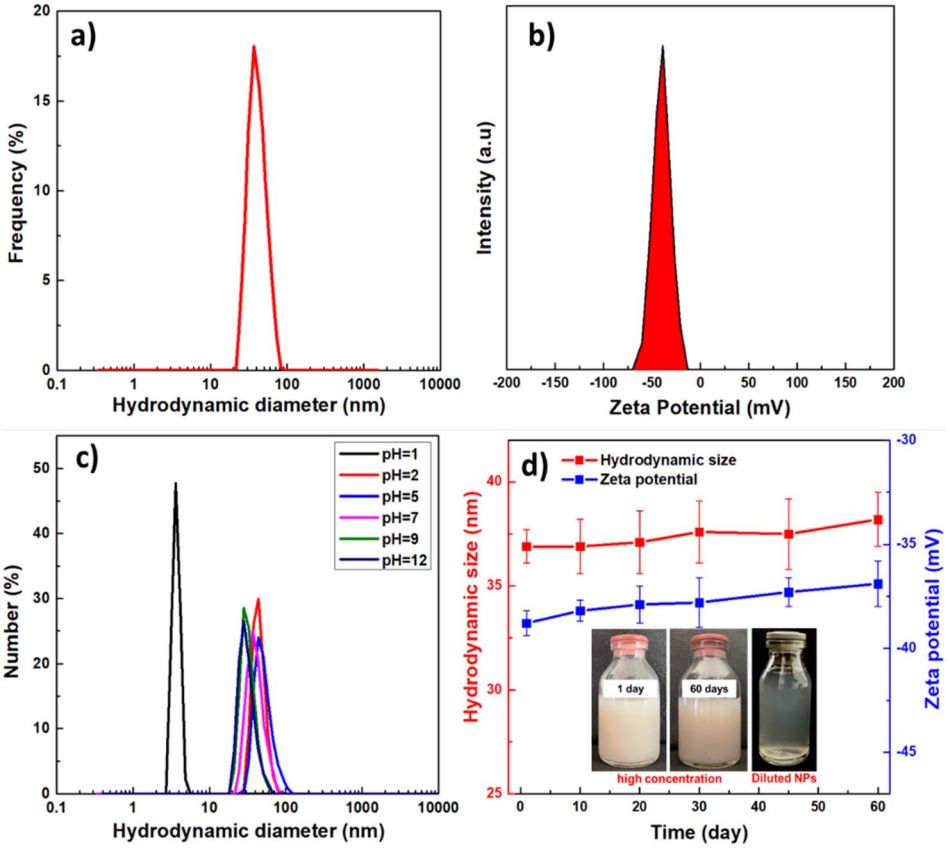

Fig. 6 (a) Hydrodynamic diameter, (b) zeta potential, (c) DLS profiles of Bi/Bi_2O_3@PAA NPs at different pH values and (d) long-term colloidal stability of the NPs over time, with corresponding solution photographs (inset).

increasing Bi concentrations, indicating a concentration-dependent enhancement in X-ray attenuation.

This effect arises from the increasing density of high atomic number atoms (Bi^{3+}) in the medium, as CT contrast is directly correlated with the concentration of contrast-generating atoms within a given volume. Quantitative analysis revealed a linear relationship between the Hounsfield unit (HU) values and Bi concentration, with a calculated slope of 14.32 ± 1.14 HU mM^{-1} at 80 kV. This value exceeds that of several iodine-based clinical contrast agents and previously reported Bi-based agents, as summarized in Table 1.

While Table 1 shows that several Bi-based agents with larger particle sizes exhibited lower CT numbers than those obtained in our study, the work by Tarighatnia *et al.*,[28] which reported Bi NPs with an average size of 32.17 nm, demonstrated higher CT numbers under similar concentration conditions. In our study, the effect of particle size on CT contrast was not systematically investigated and thus was not a primary focus of the discussion.

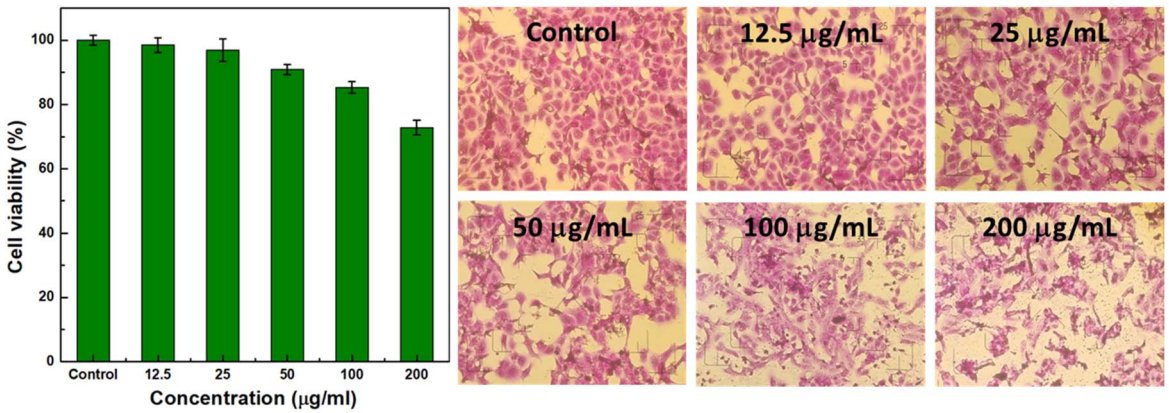

Fig. 7 Cellular cytotoxicity in Vero cells after 72 h incubation.

© 2025 The Author(s). Published by the Royal Society of Chemistry

Open Access Article. Published on 28 May 2025. Downloaded on 2/18/2026 10:23:10 AM.
This article is licensed under a Creative Commons Attribution-NonCommercial 3.0 Unported Licence.

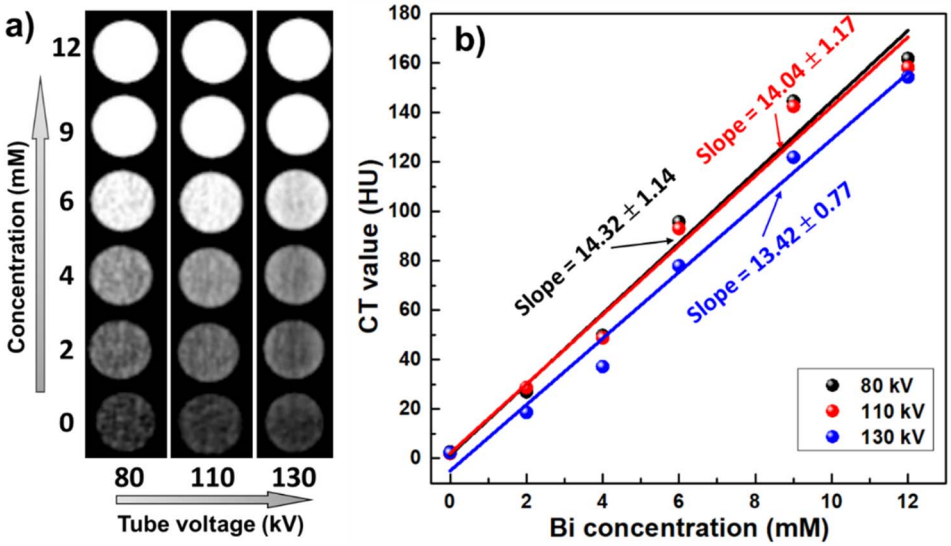

Fig. 8 (a) *In vitro* CT images and (b) corresponding CT signals curves of Bi/Bi_2O_3@PAA with different concentration under different tube ranging from 80 to 130 kV.

Nonetheless, the observed discrepancies suggest that nanoparticle size may influence CT attenuation.

To date, the literature has reported conflicting findings regarding the relationship between NP size and CT contrast. For instance, Xu *et al.*[55] and Khademi *et al.*[56] found that smaller Au NPs (<60 nm) exhibited higher X-ray attenuation than larger ones, possibly due to improved dispersion and higher surface-to-volume ratios. In contrast, Dou *et al.* observed that larger Au NPs produced greater contrast, possibly due to size-dependent variations in the spatial distribution of Bi atoms that influence the frequency of secondary atomic interactions.[57] Meanwhile, Ross *et al.* reported size-independent attenuation for Au NPs up to 76 nm.[58] Similarly, Dong *et al.* concluded that no statistically significant difference in CT contrast was observed across Au NPs of various sizes (4–152 nm) in phantom imaging using different CT systems, as the mass concentration of attenuating material remained constant regardless of particle size.[59] These inconsistencies highlight that CT contrast is not determined solely by NP size, but rather by a combination of physicochemical factors. Parameters such as surface coating, hydration state, dispersion level, and colloidal stability can all influence effective electron density and, consequently, X-ray attenuation. For instance, smaller particles may form overly fine dispersions or acquire thick hydration layers, reducing their X-ray blocking efficiency.

Table 1 Summary of Hounsfield unit (HU) values for various iodine- and Bi-based contrast agents

Contrast agent	Morphology, size (nm)	CT value (HU mM^{-1})	Tube voltage (kV_p)	References
Bi/Bi_2O_3@PAA NPs	**Spherical, 3.0**	**14.32**	**80**	**This work**
		14.04	**110**	
		13.42	**130**	
Bi_2O_3@PAA NPs	Spherical, 2.3	11.7	70	4
Bi_2O_3@dextran NPs	Spherical, 3.4	6.945	80	22
		5.837	120	
Bi_2S_3@polyvinyl pyrrolidone (PVP)	Nanosheet, (10–50) × (3–4)	9.7	50	48
Bi@poly(DL-lactic-*co*-glycolic acid)	Spherical, 38	6.6	80	49
		5.3	120	
Bi@1,2-propanediol and glucose	Faceted, 74	5.9	80	50
Bi@Oligosaccharide	Spherical, 22	8.5	80	51
		6.4	120	
Bi@PVP nanodot	Spherical, 2.7	7.064	120	52
Bi-SR-PEG NPs	Spherical, 40	6.1	120	53
Bi-DTPA chelate	NA	7.3	120	54
Ultravist	NA	4.4	70	4
Iobitridol	NA	3.850	120	52
Iohexol	NA	4.88	120	53

© 2025 The Author(s). Published by the Royal Society of Chemistry

Open Access Article. Published on 28 May 2025. Downloaded on 2/18/2026 10:23:10 AM. This article is licensed under a Creative Commons Attribution-NonCommercial 3.0 Unported Licence.

To better elucidate the influence of Bi NP size on CT contrast, we plan to conduct controlled experiments in future studies that isolate particle size while keeping other variables constant.

Additionally, the effect of tube voltage on CT attenuation was evaluated across all tested Bi concentrations. The results showed a slight decrease in CT numbers with increasing tube voltage, which is a common trend attributed to the diminished contribution of the photoelectric effect at higher photon energies. Nevertheless, the CT attenuation values of Bi/Bi_2O_3@PAA NPs remained relatively stable across the voltage range, which can be attributed to the high K-edge energy of bismuth (90.5 keV). These findings suggest that Bi/Bi_2O_3@PAA NPs offer superior and voltage-independent CT imaging performance compared to conventional iodine-based contrast agent.

Our study demonstrates the potential of the synthesized ultrasmall Bi/Bi_2O_3 NPs as promising CT contrast agents, supported by favorable physicochemical characteristics and strong *in vitro* imaging performance. However, there are several limitations. For example, *in vivo* studies were not conducted, so biodistribution, clearance, and safety profiles remain unclear. Cellular uptake was not assessed, limiting insights into nanoparticle–cell interactions. Moreover, although the NPs showed good CT contrast, the effect of particle size on CT attenuation was not systematically explored. Future studies addressing these limitations are necessary to further validate and optimize their biomedical application.

Conclusions

In summary, we successfully synthesised ultrasmall Bi/Bi_2O_3 NPs using straightforward one-pot thermal decomposition method, yielding a core–shell structure. Surface modification with polyacrylic acid (PAA) further improved the aqueous dispersibility and biocompatibility of the NPs, enabling their suitability for biomedicine. The resulting Bi/Bi_2O_3@PAA NPs exhibited excellent X-ray attenuation performance, with Hounsfield unit (HU) values surpassing those of the conventional iodine-based contrast agents. Owing to their ultra-small size, high Bi content, superior stability, and low cytotoxicity, Bi/Bi_2O_3@PAA NPs present a promising alternative to traditional iodine-based CT contrast agents. Their facile synthesis and outstanding imaging properties highlight their potential for future clinical translation in diagnostic imaging.

Data availability

The data supporting this article have been included in the main text and as part of the ESI.†

Author contributions

Le T. T. Tam conceptualized the study, designed the methodology and drafted the manuscript. Duong T. Ngoc, Nguyen T. Yen and Nguyen T. Suong conducted the experiments and collected the associated data. Nguyen T. N. Linh carried out the toxicity tests and collected the associated data, while Le T. Tam and Nguyen V. Dong performed the CT measurements. Ngo T. Dung and Le T. Lu acquired funding and supervised the overall project. All authors reviewed and approved the final version of the manuscript.

Conflicts of interest

There are no conflicts to declare.

Acknowledgements

This research was financially supported by the Development program in the Field of Physics for the 2021–2025 period, through the Ministry of Science and Technology of Vietnam (Grant Number: ĐTĐL.CN.16/23). Le Thi Thanh Tam was funded by the Master, PhD Scholarship Programme of Vingroup Innovation Foundation (code: VINIF.2023.TS.104).

References

1 C. H. McCollough, S. A. Leng, L. F. Yu and J. G. Fletcher, *Radiology*, 2015, **276**, 637–653.
2 H. Bi, F. He, Y. Dong, D. Yang, Y. Dai, L. Xu, R. Lv, S. Gai, P. Yang and J. Lin, *Chem. Mater.*, 2018, **30**, 3301–3307.
3 H. Lusic and M. W. Grinstaff, *Chem. Rev.*, 2013, **113**, 1641–1666.
4 A. Ghazanfari, S. Marasini, X. Miao, J. A. Park, K. H. Jung, M. Y. Ahmad, H. Yue, S. L. Ho, S. Liu, Y. J. Jang, K. S. Chae, Y. Chang and G. H. Lee, *Colloids Surf., A*, 2019, **576**(5), 73–81.
5 C. H. Hunt, R. P. Hartman and G. K. Hesley, *Am. J. Roentgenol.*, 2009, **193**, 1124–1127.
6 K. Ai, Y. Liu, J. Liu, Q. Yuan, Y. He and L. Lu, *Adv. Mater.*, 2011, **23**, 4886–4891.
7 N. Gharehaghaji, B. Divband and F. Bakhtiari-Asl, *BioNanoScience*, 2020, **10**, 909–916.
8 M. Yektamanesh, Y. Ayyami, M. Ghorbani, M. Dastgir, R. Malekzadeh and T. Mortezazadeh, *Int. J. Pharm.*, 2024, **659**, 124264.
9 C. Xu, Y. L. Wang, C. Y. Zhang, Y. W. Jia, Y. J. Luo and X. Y. Gao, *Nanoscale*, 2017, **9**, 4620–4628.
10 J. R. Ashton, K. D. Castle, Y. Qi, D. G. Kirsch, J. L. West and C. T. Badea, *Theranostics*, 2018, **8**, 1782–1797.
11 Z. Li, J. Liu, Y. Hu, Z. Li, X. Fan, Y. Sun, F. Besenbacher, C. Chen and M. Yu, *Biomaterials*, 2018, **161**, 279–291.
12 R. Malekzadeh, M. Ghorbani, P. Faghani, B. B. Abdollahi, T. Mortezazadeh and B. Farhood, *J. Radiat. Res. Appl. Sci.*, 2023, **16**, 100490.
13 B. M. Yeh, P. F. FitzGerald, P. M. Edic, J. W. Lambert, R. E. Colborn, M. E. Marino, P. M. Evans, J. C. Roberts, Z. J. Wang, M. J. Wong and P. J. Bonitatibus, *Adv. Drug Delivery Rev.*, 2017, **113**, 201–222.
14 D. M. Griffith, H. Y. Li, M. V. Werrett, P. C. Andrews and H. Z. Sun, *Chem. Soc. Rev.*, 2021, **50**, 12037–12069.
15 W. C. Huang, J. Zhu, M. K. Wang, L. P. Hu, Y. F. Tang, Y. Q. Shu, Z. J. Xie and H. Zhang, *Adv. Funct. Mater.*, 2021, **31**, 2007584.

© 2025 The Author(s). Published by the Royal Society of Chemistry

Open Access Article. Published on 28 May 2025. Downloaded on 2/18/2026 10:23:10 AM. This article is licensed under a Creative Commons Attribution-NonCommercial 3.0 Unported Licence.

16 H. Yu, H. Guo, Y. Wang, Y. Wang and L. Zhang, *Wiley Interdiscip. Rev.:Nanomed. Nanobiotechnol.*, 2022, **14**, e1801.
17 W. Liao, P. Lei, J. Pan, C. Zhang, X. Suna, X. Zhang, C. Yu and S. K. Sun, *Biomaterials*, 2019, **203**, 1.
18 J. Fu, J. Guo, A. Qin, X. Yu, Q. Zhang, X. Lei, Y. Huang, M. Chen, J. Li, Y. Zhang, J. Liu and Y. Dang, *J. Nanobiotechnol.*, 2020, **18**, 110.
19 G. Shu, L. Zhao, F. Li, Y. Jiang, X. Zhang, C. Yu, J. Pan and S. K. Sun, *Biomaterials*, 2024, **305**, 122422.
20 G. D. Dai, Y. Zhang, X. M. Wang, X. Y. Wang, J. Jia, F. Jia, L. Yang and C. M. Yang, *Front. Oncol.*, 2022, **12**, 813955.
21 X. Yu, A. Li, C. Zhao, K. Yang, X. Chen and W. Li, *ACS Nano*, 2017, **11**(4), 3990–4001.
22 G. Shu, C. Zhang, Y. Wen, J. Pan, X. Zhang and S. K. Sun, *Biomaterials*, 2024, **311**, 122658.
23 J. M. Kinsella, R. E. Jimenez, P. P. Karmali, A. M. Rush, V. R. Kotamraju, N. C. Gianneschi, E. Ruoslahti, D. Stupack and M. J. Sailor, *Angew. Chem., Int. Ed.*, 2011, **50**, 12308–12311.
24 J. Chen, X. Q. Yang, Y. Z. Meng, M. Y. Qin, D. M. Yan, Y. Qian, G. Q. Xu, Y. Yu, Z. Y. Ma and Y. D. Zhao, *Chem. Commun.*, 2013, **49**, 11800–11802.
25 Y. Wang, Y. Y. Wu, Y. J. Liu, J. Shen, L. Lv, L. B. Li, L. C. Yang, J. F. Zeng, Y. Y. Wang, L. S. W. Zhang, Z. Li, M. Y. Gao and Z. F. Chai, *Adv. Funct. Mater.*, 2016, **26**, 5335–5344.
26 Y. Lu, L. H. Li, Z. F. Lin, M. Li, X. M. Hu, Y. Zhang, M. Y. Peng, H. Xia and G. Han, *Adv. Healthcare Mater.*, 2018, **7**, 1800602.
27 C. Yang, C. Guo, W. Guo, X. Zhao, S. Liu and X. Han, *ACS Appl. Nano Mater.*, 2018, **1**, 820–830.
28 A. Tarighatnia, M. H. Abdkarimi, N. D. Nader, T. Mehdipour, M. R. Fouladi, A. Aghanejad and H. Ghadiri, *New J. Chem.*, 2021, **45**, 18871.
29 A. Tarighatnia, M. R. Fouladi, M. R. Tohidkia, G. Johal, N. D. Nader, A. Aghanejad and H. Ghadiri, *J. Drug Delivery Sci. Technol.*, 2021, **66**, 102895.
30 M. A. Shahbazi, L. Faghfouri, M. P. A. Ferreira, P. Figueiredo, H. Maleki, F. Sefat, J. Hirvonen and H. A. Santos, *Chem. Soc. Rev.*, 2020, **49**, 1253–1321.
31 C. Gomez, G. Hallot and S. Laurent, *Pharmaceutics*, 2021, **13**(11), 1793.
32 L. Dong, P. Zhang, X. Liu, R. Deng, K. Du, J. Feng and H. Zhang, *ACS Appl. Mater. Interfaces*, 2019, **11**(8), 7774–7781.
33 L. Jiao, Q. X. Li, J. J. Deng, N. Okosi, J. F. Xia and M. Su, *Nanoscale*, 2018, **10**, 6751–6757.
34 M. Mohammadi, A. Tavajjohi, A. Ziashahabi, N. Pournoori, S. Muhammadnejad, H. Delavari and R. Poursalehi, *Nano-Micro Lett.*, 2019, **14**, 239–244.
35 C. Li, K. P. O'Halloran, H. Ma and S. Shi, *J. Phys. Chem. B*, 2009, **113**, 8043–8048.
36 X. Liu, H. Cao and J. Yin, *Nano Res.*, 2011, **4**(5), 470–482.
37 S. Dadashi, R. Poursalehi and H. Delavari, *Mater. Res. Bull.*, 2018, **97**, 421–427.
38 S. S. Shaker, R. A. Ismail and D. S. Ahmed, *J. Inorg. Organomet. Polym. Mater.*, 2022, **32**, 1381–1388.
39 Z. Feng, Y. Fu, Z. Yang, Y. He, C. Feng, B. Gao, P. Zhang, X. An, A. Abudula and G. Guan, *J. Colloid Interface Sci.*, 2025, **678**, 913–923.
40 Z. Yang, X. An, Z. Feng, Y. Ramli, C. Feng, P. Wang, J. Wang, S. Li, X. Hao, H. Lu, A. Abudula and G. Guan, *Sep. Purif. Technol.*, 2025, **354**, 129205.
41 S. Singh, R. K. Sahoo, N. M. Shinde, J. M. Yun, R. S. Mane, W. Chung and K. H. Kim, *RSC Adv.*, 2019, **9**, 32154–32164.
42 L. J. Treadwell, T. J. Boyle, N. S. Bell, M. A. Rodriguez, B. R. Muntifering and K. Hattar, *J. Mater. Sci.*, 2017, **52**, 8268–8279.
43 M. T. Nguyen, K. Wongrujipairoj, H. Tsukamoto, S. Kheawhom, S. Mei, V. Aupama and T. Yonezawa, *ACS Sustainable Chem. Eng.*, 2020, **8**, 18167–18176.
44 N. T. T. Khue, L. T. T. Tam, N. T. Dung, L. T. Tam, N. X. Chung, N. T. N. Linh, N. D. Vinh, B. M. Quy and L. T. Lu, *ChemistrySelect*, 2022, **7**(34), e202202062.
45 T. Placido, L. Tognaccini, B. D. Howes, A. Montrone, V. Laquintana, R. Comparelli, M. L. Curri, G. Smulevich and A. Agostiano, *ACS Omega*, 2018, **3**, 4959–4967.
46 M. Sarani, M. Roostaee, M. Adeli-Sardou, D. Kalantar-Neyestanaki, S. A. A. Mousavi, A. Amanizadeh, M. Barani and A. Amirbeigi, *J. Trace Elem. Med. Biol.*, 2024, **81**, 127325.
47 M. Prakash, H. P. Kavitha, S. Arulmurugan, J. P. Vennila, S. Abinaya, D. Lohita and R. Suresh, *J. Sol-Gel Sci. Technol.*, 2024, **110**, 807–818.
48 O. Rabin, J. M. Perez, J. Grimm, G. Wojtkiewicz and R. Weissleder, *Nat. Mater.*, 2006, **5**, 118–122.
49 E. R. Swy, A. S. Schwartz-Duval, D. D. Shuboni, M. T. Latourette, C. L. Mallet, M. Parys, D. P. Cormode and E. M. Shapiro, *Nanoscale*, 2014, **6**, 13104–13112.
50 A. L. Brown, P. C. Naha, V. Benavides-montes, H. I. Litt, A. M. Goforth and D. P. Cormode, *Chem. Mater.*, 2014, **26**, 2266–2274.
51 B. Wei, X. Zhang, C. Zhang, Y. Jiang, Y. Y. Fu, C. Yu, S. K. Sun and X. P. Yan, *ACS Appl. Mater. Interfaces*, 2016, **8**, 12720–12726.
52 P. Lei, R. An, P. Zhang, S. Yao, S. Song, L. Dong, X. Xu, K. Du, J. Feng and H. Zhang, *Adv. Funct. Mater.*, 2017, 1702018.
53 N. Yu, Z. Wang, J. Zhang, Z. Liu, B. Zhu, J. Yu, M. Zhu, C. Peng and Z. Chen, *Biomaterials*, 2018, **161**, 279–291.
54 J. Fu, J. Guo, A. Qin, X. Yu, Q. Zhang, X. Lei, Y. Huang, M. Chen, J. Li, Y. Zhang, J. Liu, Y. Dang, D. Wu, X. Zhao, Z. Lin, Y. Lin, S. Li and L. Zhang, *J. Nanobiotechnol.*, 2020, **18**, 110.
55 C. Xu, G. A. Tung and S. Sun, *Chem. Mater.*, 2008, **20**, 4167–4169.
56 S. Khademi, S. Sarkar, S. Kharrazi, S. M. Amini, A. Shakeri-Zadeh, M. R. Ay and H. Ghadiri, *Phys. Med.*, 2018, **45**, 127–133.
57 Y. Dou, Y. Guo, X. Li, X. Li, S. Wang, L. Wang, G. Lv, X. Zhang, H. Wang, X. Gong and J. Chang, *ACS Nano*, 2016, **10**, 2536–2548.
58 R. D. Ross, L. E. Cole, J. M. R. Tilley and R. K. Roeder, *Chem. Mater.*, 2014, **26**, 1187–1194.
59 Y. C. Dong, M. Hajfathalian, P. S. N. Maidment, J. C. Hsu, P. C. Naha, S. Si-Mohamed, M. Breuilly, J. Kim, P. Chhour, P. Douek, H. I. Litt and D. P. Cormode, *Sci. Rep.*, 2019, **9**, 14912.

© 2025 The Author(s). Published by the Royal Society of Chemistry